

Helicopter Radar Return Analysis: Estimation and Blade Number Selection

Pawan Setlur, Fauzia Ahmad, and Moeness Amin
Radar Imaging Lab, Center for Advanced Communications,
Villanova University, Villanova, PA 19085, USA.
E-mail: {pawan.setlur, fauzia.ahmad, moeness.amin}@villanova.edu

Abstract—The problem of helicopter parameter estimation and blade number selection is addressed. The parameters are estimated based on Maximum Likelihood methods, and the corresponding Cramér-Rao bounds are derived. To avoid ambiguities in blade number estimation, we apply information theoretic criteria for blade number selection incorporating alternate penalty functions. We assume that a clutter filter essentially removes all of the clutter and also part of the signal returns, lowering the effective signal-to-noise-ratio. The Fractional Fourier Transform is used to separate the combined tail and main rotor signals into two different returns, allowing initial estimates of their corresponding rotor parameters. The proposed technique is validated by using returns from a helicopter observed experimentally with a pulse-Doppler radar.

Keywords- Micro-Doppler, Rotor blades, pseudo maximum likelihood, model selection, time-frequency, radar.

1. Introduction

When an emitted radar signal interacts with a translating target, it undergoes the well known Doppler effect, i.e., the received carrier frequency is shifted by an amount proportional to the radial velocity of the target. In addition to translation, if the target or structures on the target are vibrating or rotating, the returned signal has the main Doppler shift along with other non-linear and possibly periodic sideband modulations referred to as micro-Doppler (MD) [1, 2]. These target-specific micro-motions provide additional features which aid in target identification. The MD resulting from engine vibrations was used to detect and identify a tank in [3]. In [4], the MD has been used to identify the natural resonant frequency of a tractor-trailer. For airborne targets, the presence of MD due to the rotating tail and main rotor blades in helicopters, and from the turbine engines of planes, is shown to offer unique opportunities for target classification and recognition [4, 5].

One of the important features for target recognition is the radar cross section (RCS). The target RCS varies with several factors, including frequency, aspect angle, and geometry of the target itself. The RCS based identification may fail to identify the helicopters due to geometrical similarities [6]. However, distinction between rotorcrafts can be drawn based on blade rotor counts and respective rotational rates.

In this paper, we focus on radar returns from a helicopter. It is noted that a helicopter has three main scattering centers, namely the main body, the main rotor, and the smaller tail rotor. The returns from the main helicopter body almost mask the smaller returns from the other two scattering centers [3]. The main body of a helicopter has a large RCS and can easily be seen by simple Fourier techniques applied to the radar returns [3], [7-10]. We focus on the distinct features, namely those associated with the main and tail rotor assemblies. The main rotor in a helicopter pushes the air downwards creating a vertical lift, and causes the main torque, whereas the tail rotor provides the anti torque to compensate for the main torque. The main and the tail rotor blades obviously cannot have one blade each and their respective blade counts can be anywhere between two to eight [11]. Unlike traditional Swerling type models, it was shown that the RCS of helicopter rotor returns have a deterministic structure, which depends on the rotational frequency

of the rotor [9, 12, 13]. Helicopter radar echoes, dealing with continuous wave (CW) radars, have been studied for many years [14-17]. In [14], the echoes were analyzed either in the time-domain or the frequency domain, but not jointly in the TF domain. In [15], a bistatic CW radar was used to study the helicopter bistatic radar returns. In [16], the radar returns were analyzed using the short time Fourier transform (STFT), and it was determined that the rotation rate of the blades can be properly estimated given the true blade number. However, no method was provided to perform blade number selection. In [17], the authors use TF as well as tomographic techniques to estimate the parameters in the helicopter signal model.

The main thrust of this paper is the estimation of the rotor rotation frequency, the blade diameter, and the number of blades from an unknown helicopter under radar surveillance. The parameters are estimated based on Maximum Likelihood (ML) methods, and the corresponding Cramér-Rao bounds (CRBs) are derived. To avoid ambiguities in blade number estimation, we apply information theoretic criteria for blade number selection incorporating alternate penalty functions. We assume that a simple clutter excision filter is used which may reduce the effective signal-to-noise-ratio (SNR) of the signal.

The paper is organized as follows, Section 2 describes the signal model, while Section 3 discusses some typical estimation techniques. In Section 4, we present the optimal model selection or blade number selection techniques which are related to the information theoretic criteria (ITC). The CRBs are derived in Section 5, and the simulations and experimental results are presented in Section 6.

2. Signal Model

We adopt the signal model derived in [9, 13]. For simplicity, we ignore the contribution of the tail rotor as its returns are similar in structure to the main rotor [9]. The main rotor blades have a large diameter as compared to the tail rotor, and the rotational frequency of the tail rotor is generally much higher than that of the main rotor. It is noted that in general, the main rotor has a larger RCS than the tail rotor [6].

Typical blades are aerofoils having a bending, twisting, and turning motion. For analytical tractability, we model the blades as homogenous rigid rods rotating about a fixed axis at a constant rotation rate [3, 9].

As in [9], we assume that the radar sends a continuous wave signal at carrier frequency f . The transmitted signal interrogates a helicopter with K unknown rotor blades. The received baseband signal at discrete time n is expressed as,

$$\begin{aligned} x(n) &= \rho \exp(j\omega_d n + j\theta) \times \sum_{k=1}^K h_k(n) \exp(j4\pi f d \cos(\omega_o n - \phi_k) / c) + v(n) + u(n) \\ &= s(n) + v(n) + u(n) \end{aligned} \quad (1)$$

where ω_d denotes the Doppler frequency. The rotational frequency of the blade is represented as ω_o . The parameter $d = L \cos(\beta) / 2$ is proportional to one half of the radius of the blade, L , and is analogous to the modulation index [9, 12]. The aspect angle is denoted as β , and can be estimated if the radar has an aperture associated with it, and is not the subject of this paper. The parameter ϕ_k denotes the phase term in the signal return, whereas parameter ρ is an arbitrary amplitude and θ is its phase. The function $h_k(n)$ captures the cyclic RCS fluctuations of the k -th rotor blade, and can be modeled as [9, 12, 13]

$$h_k(n) = \text{sinc}\left(\frac{4\pi f d \cos(\omega_o n - \phi_k)}{c}\right) \quad (2)$$

In (1), $v(n)$ is an additive noise which is assumed to be a white circular uncorrelated complex Gaussian random process of variance σ^2 . The clutter is modeled by a random process denoted as $u(n)$, whose power spectral density (PSD) is finite, and has a support symmetric around DC. The clutter spectrum overlaps partially with the frequency support of the signal $s(n)$. The return in (1) is filtered using a clutter filter whose transfer function is denoted as $G(\omega)$, and is assumed to be

$$G(\omega) = \begin{cases} 0, & |\omega| \leq \omega_{cl} \\ 1, & \text{otherwise} \end{cases} \quad (3)$$

where ω_{cl} is the cut-off frequency. The filtered signal is represented by the convolution $y(n) = g(n) * x(n)$, and will be used from hereon in parameter estimation. The blades are placed symmetrically around the rotor, in which case

$$\phi_k = \phi_o + 2\pi(k-1) / K, \quad k = 1, 2, \dots, K \quad (4)$$

where ϕ_o is a deterministic phase at the first time instant. With (4) in effect, the Fourier transform of the noise and clutter-free return $s(n)$ is given by

$$S(\omega) = \sum_{m=-M}^{m=M} z(d, \phi_o, m) \delta(m - \omega_d - M\omega_o) \quad (5)$$

where $z(\cdot)$ is a function which incorporates Bessel functions of the first kind [9, pg. 189]. From (3) and (5), it is evident that the filtered return $y(n)$ has a frequency support over the interval $[-M\omega_o + \omega_d, -\omega_{cl}]$ for the negative frequencies and $[\omega_{cl}, M\omega_o + \omega_d]$ for the positive frequencies. The objective is to estimate the set of parameters $\boldsymbol{\psi} = [\omega_o, \omega_d, d, \phi_o, \rho, \theta, \sigma^2]$ and the correct blade number K .

3. Parameter Estimation

Assume clutter free radar returns and no clutter filter is applied i.e., $y(n) = s(n) + v(n)$. Then, the method of ML culminates to a non-linear least squares (NLS) cost function given by [18],

$$(\hat{\omega}_d, \hat{\omega}_o, \hat{d}, \hat{\phi}_o) = \arg \max_{(\omega_d, \omega_o, d, \phi_o)} J(\omega_d, \omega_o, d, \phi_o) = \arg \max_{(\omega_d, \omega_o, d, \phi_o)} \mathbf{y}^H \mathbf{P} \mathbf{y}, \quad (6)$$

$$\mathbf{y} = [y(0), y(1), \dots, y(N-1)]^T$$

where

$$\mathbf{P} = \mathbf{A}(\mathbf{A}^H \mathbf{A})^{-1} \mathbf{A}^H, \mathbf{A} = [\mathbf{a}_1, \mathbf{a}_2, \dots, \mathbf{a}_K],$$

$$\mathbf{a}_k := \boldsymbol{\gamma} \odot \mathbf{e}_k, \mathbf{e}_k := [h_k(0)e^{j4\pi fd \cos(\phi_k)/c}, h_k(1)e^{j4\pi fd \cos(\omega_o(1-\phi_k)/c)}, \dots, h_k(N-1)e^{j4\pi fd \cos(\omega_o(N-1-\phi_k)/c)}]^T \quad (7)$$

$$\boldsymbol{\gamma} := [1, e^{j\omega_d}, \dots, e^{j\omega_d(N-1)}]^T$$

In (7), the Hadamard product is defined as ' \odot '. Note that (6) depends on the number of blades K , which is unknown. One can derive the estimates $\hat{\rho}$ and $\hat{\theta}$ in a straightforward manner after obtaining the estimates in (6). It is noted that, due to the effect of the clutter filter, if (6) is used with the clutter filtered return, then the method corresponds to pseudo ML (PML) [19].

3.1. Initialization techniques for estimation

To obtain an initial estimate of the rotational frequency, we consider the autocorrelation sequence $r(\tau)$ of the clutter filtered signal $y(n)$, as a function of the discrete lag τ . It is shown in [3] that apart from the

obvious zeroth lag, the autocorrelation peaks at lags which are integer multiples of the inverse of the rotational frequency times K . Figure 1(a) shows the correlation sequence for a 3-blade helicopter for 10 dB SNR after clutter filtering. Figure 1(b) depicts the corresponding results for a 4-blade helicopter. In Fig. 1(a), the clutter in the normalized frequency band between $\pm 0.1 \times \pi$ rad/sample is assumed. The Doppler radar operates at 0.9 GHz with the target moving at 10m/s. The rotation rate of the blades is 100 rpm, and the diameter of the blades is set equal to 12m. The correlation sequence is provided using time averaging. For Fig. 1(b), the rotational frequency used was one half of that used in Fig. 1(a); the rest of the parameters are the same. Let τ_1, τ_2, \dots , denote the time-lags corresponding to the peak values, then $\omega_{oK} = K \omega_o$ can be estimated as

$$\hat{\omega}_{oK} = 2\pi / (\hat{\tau}_{q+1} - \hat{\tau}_q), \text{ or } \hat{\omega}_{oK} = 2\pi q / \hat{\tau}_q, \quad q = 1, 2, \dots \quad (8)$$

The correlation sequence is quite robust to noise, and provides accurate estimates of ω_{oK} [3]. In the presence of both the main and the tail rotor, the correlation sequence may have several peaks and can suffer from the strong return dominating the weak return. In such cases, the signal may be separated into the respective tail and main rotor components using wavelets [3], or the Fractional Fourier transform (FrFT), which is the approach taken in this paper. Estimation of the correlation peaks corresponding to the main and tail rotor blades can then separately follow. Considering the estimation of ω_d , when $\omega_d = 0$, the spectrum $S(\omega)$ is symmetric around DC. However, when $\omega_d \neq 0$, the spectrum is shifted either to the left or to the right depending on the sign of ω_d . The bandwidth extent of the signal can then be used to obtain a crude estimate of ω_d . Denote BW_+ as the frequency corresponding to the maximum positive support of $S(\omega)$, and likewise, BW_- corresponds to the minimum negative support of $S(\omega)$. The estimate $\hat{\omega}_d$ can then be provided as,

$$\hat{\omega}_d = \pi \times (\hat{BW}_+ + \hat{BW}_-) \quad (9)$$

The parameters BW_{\pm} can be obtained by reading off of the spectrum of the returns, or simply by computing the frequency bands which capture a large specific percentage of the signal energy.

There are other techniques for estimating ω_d and ω_{oK} , based on least squares [20] and on the harmonic MUSIC algorithm [21]. These techniques require the dimension of the signal subspace, which is unknown and may assume a very large value.

If ‘ K ’, the true blade number, is known, the initial estimates for (d, ϕ_o) can then be computed using a grid search of the ML cost function designed for a single blade, and can be estimated as

$$\begin{aligned}
 (\hat{d}, \hat{\phi}_o) &= \arg \max_{d, \phi_o} Q(d, \phi_o, \hat{\omega}_d, \hat{\omega}_o) \\
 Q(d, \phi_o, \omega_d, \omega_o) &:= \frac{\left\| \sum_{n=0}^{N-1} y(n) \exp(-j\omega_d n) \text{sinc}(\psi(n)) \exp(-j\psi(n)) \right\|^2}{\sum_{n=0}^{N-1} \text{sinc}^2(\psi(n))} \\
 \psi(n) &:= 4\pi f d \cos(\omega_o n - \phi_o) / c
 \end{aligned} \tag{10}$$

The function $Q(\cdot)$ depends on prior estimates of the Doppler frequency, which is obtained from (9), and the rotational frequency, which is obtained from (8).

We examine the time-frequency signal representation of the blade return signal. The spectrograms are shown in Fig. 2. A key observation is that

$$\begin{aligned}
 &\text{if } K \text{ even,} \\
 &\exists \omega' : |TFD(n, \omega + \omega')| = |TFD(n, \omega' - \omega)|, \forall n = 0, 1, \dots, N-1, \omega \in (-\pi, \pi] \\
 &\text{if } K \text{ odd,} \\
 &\nexists \omega' : |TFD(n, \omega + \omega')| = |TFD(n, \omega' - \omega)|, \forall n = 0, 1, \dots, N-1, \omega \in (-\pi, \pi]
 \end{aligned} \tag{11}$$

Equation (11) implies that for an even number of blades, there exists some frequency about which the time frequency distributions (TFDs) are symmetric, whereas for an odd number of blades, there exists no such frequency. In the absence of clutter, this frequency ω' is the Doppler frequency. The blade flashes represent the extrema of the instantaneous frequency, and quite clearly, for an even number of blades they are symmetric. For even blades, the receding and approaching tip of the blades coincide, as explained in [3]. It is therefore straightforward to determine if K is even or odd from a mere inspection of the TFDs. If the blades are even, we are only left with deciding whether $K = 2, 4, \dots$, and if it is odd, then $K = 3, 5, \dots$.

Consider the estimates

if K is even

$$(\hat{K}, \hat{d}, \hat{\phi}_o) = \arg \max_{k, d, \phi_o} (Q(d, \phi_o, \hat{\omega}_d, \hat{\omega}_{oK} / 2), Q(d, \phi_o, \hat{\omega}_d, \hat{\omega}_{oK} / k), \dots), k = 4, 6, \dots$$

if K is odd

$$(\hat{K}, \hat{d}, \hat{\phi}_o) = \arg \max_{k, d, \phi_o} (Q(d, \phi_o, \hat{\omega}_d, \hat{\omega}_{oK} / 3), Q(d, \phi_o, \hat{\omega}_d, \hat{\omega}_{oK} / k), \dots), k = 5, 7, \dots$$

$$\hat{\omega}_o = \hat{\omega}_{oK} / \hat{K}$$

(12)

Equation (12) is evaluated using a grid search. As evident from Fig. 3, the solution to the above equation can have several local maxima. For example in a ‘2’ blade problem, (12) may results in an estimate of 2, 4, 6, or 8 blades, for low SNRs. One particular realization is shown in Fig. 4. To avoid the problem of local maxima, we first estimate the approximate locations of the maxima for given values of K , i.e.,

If K is even

$$(\hat{d}_k, \hat{\phi}_{ok}) = \arg \max_{d, \phi_o} Q(d, \phi_o, \hat{\omega}_d, \hat{\omega}_{oK} / k), k = 2, 4, \dots$$

If K is odd

$$(\hat{d}_k, \hat{\phi}_{ok}) = \arg \max_{d, \phi_o} Q(d, \phi_o, \hat{\omega}_d, \hat{\omega}_{oK} / k), k = 3, 5, \dots$$

(13)

Equation (13) can be solved using a grid search. Note that the tuple $(\hat{\omega}_{oK} / k, \hat{d}_k, \hat{\phi}_{ok})$ represents a local maximum for (6), and for the true blade number, it represents close enough estimates of the true parameters. We therefore proceed as follows. For every hypothesized k , we initialize the ML optimization in (6) with the estimates, $(\hat{\omega}_{oK} / k, \hat{d}_k, \hat{\phi}_{ok})$, and the suboptimal estimate of the Doppler, $\hat{\omega}_d$, from (9). The flowchart in Fig. 5 describes the procedure in more detail.

3.2. FrFT application: Signal with both tail and main rotor components

In practice, the tail rotor has a smaller RCS than the main rotor blade¹. In such cases, obtaining suboptimal estimates of the tail rotor from the correlation domain, as in (8), is difficult. Figure 6(a) illustrates the correlation peaks corresponding to the main rotor blade signals and weak tail rotor blade signals along with spurious peaks corresponding to the cross-correlation between the two components. In Fig. 6(a), the SNR

¹ However, in exceptional cases depending on the aspect angle and due to the twist in the main rotor shape, the tail rotor may appear to be stronger than the main rotor blades. This interesting scenario is treated in the experimental results.

is 0 dB with the main rotor being 70% stronger than the tail rotor signal. The number of blades in the main and tail rotor is 4 and 3, respectively. Figure 6(b) shows the spectrogram of the signal where the tail rotor blade flashes are barely seen. Since the flashes are impulse like, a rotation of the TF plane yields windowed sinusoids. This rotation is equivalent to applying the FrFT with parameter $\alpha = \pi / 2$ [22]. The rotation using the FrFT is shown in Fig. 7(a). Subsequent use of simple notch filters in the (Fractional Fourier) frequency domain can remove the main rotor components; the resulting signal is then rotated back by $\alpha = -\pi / 2$ by using the inverse FrFT. The spectrogram of the resulting signal along with the correlation peaks are shown in Fig. 7(b-c). Clearly both the figures show the tail rotor contributions with main rotor blade components being completely eliminated. The same procedure can be used to remove the tail rotor when it is stronger than the main rotor component, and will be demonstrated when dealing with experimental data. The FrFT procedure is described by the following steps.

1. Compute the FrFT of the original signal $x(n)$, with $\alpha = \pi / 2$.
2. Design a set of excision filters for each of the tail and main rotor component signals with respect to the fractional Fourier transformed signal.
3. Convolve the signal from step-1 with the filter's impulse responses designed to remove either the tail or the main rotor components.
4. Compute the FrFT of the resulting signal with $\alpha = -\pi / 2$. This step will undo the rotation in the TF plane.
5. The signal now is comprised of either the tail only or the main rotor only components depending on the set of filters used in step-3.
6. Repeat steps 3-5 with the different set of filters to obtain the other signal.

We wish to note that the filters for either the tail or the main rotor components are, in essence, shifted versions of one another in the spectral domain; the shift being constant and dependent on the time between flashes. In other words, one has to design only a single filter and use it to construct the other filters via frequency modulation. The FrFT procedure is used in the experimental results section.

The FrFT has several advantages when compared to traditional approaches, such as TF filtering via time-varying filters. The TF filtering approach could be used but has additional complexity due to the TF signal synthesis technique required to obtain the desired signal from the TF domain [23, 24], and references therein. The FrFT approach requires computing only two FrFTs which can be implemented efficiently using for example the algorithm in [25].

4. Model Selection (Blade Number Selection)

There are basically two approaches to model selection, the information theoretic criteria and hypothesis testing. The ITCs automatically detect the model order without resorting to thresholding, while the hypothesis tests require levels of significance and associated thresholds. More details on the hypothesis testing procedures for model selection can be found in [26]. Two of the popular ITCs are the Akaike information theoretic criterion (AIC), and the minimum description length (MDL) [27-29]. The MDL was shown to coincide with the Bayesian information criterion (BIC) [30]. The important property of the ITCs is that they are coupled with ML estimation. The well known Akaike information criteria (AIC) and the Bayesian information criteria (BIC) are defined as

$$AIC(k) := -2 \ln(p(\mathbf{x}; \hat{\boldsymbol{\psi}}, \hat{\sigma}^2)) + 2l(k), \quad BIC(k) := -\ln(p(\mathbf{x}; \hat{\boldsymbol{\psi}}, \hat{\sigma}^2)) + \frac{1}{2}l(k)\ln(N) \quad (14)$$

where $\ln(p(\mathbf{x}; \hat{\boldsymbol{\psi}}, \hat{\sigma}^2))$ is the log likelihood (LL) evaluated at the final ML estimates of $\boldsymbol{\psi}$ and σ^2 . It is noted that $\ln(p(\mathbf{x}; \hat{\boldsymbol{\psi}}, \hat{\sigma}^2))$ is a function of k , and is not shown here for notational convenience. The penalty $l(k)$ is defined as the number of free parameters in the model. The estimate for the number of the blades is then given by,

$$\hat{k}_{aic} = \arg \min_k (AIC(k)), \quad \hat{k}_{bic} = \arg \min_k (BIC(k)), \quad k \in \{1, 2, 3, \dots, K\} \quad (15)$$

For the problem at hand, since the noise is complex Gaussian, the negative LL cost function can be further simplified to

$$-\ln(p(\mathbf{x}; \hat{\boldsymbol{\psi}}, \hat{\sigma}^2)) = N \ln(\hat{\sigma}^2) \quad (16)$$

With (4) in effect, $\boldsymbol{\psi} = [\omega_d, \omega_o, d, \phi_o, \rho, \theta, \sigma^2]^T$, and we readily obtain the constant value $l(k) = 7$. This implies that the penalty term in (14) can be omitted entirely. In this case, AIC and BIC give the same model order, which depends entirely on the log likelihood evaluated for each model order. However, it is well known that the ML tends to select the model with the highest complexity [31]. This was also validated from our extensive simulations. As an example, if we evaluate the ML in (6) for say $K = 8$, for a rotor with 2 blades, the LL cost function will assume a minimum value corresponding to 8 blades, and will yield smaller values for 6 and 4 blades, than the 2 blades. Some representative blade orientations for 2, 4, 6, and 8 blades for this example are shown in Fig. 8.

The above inherent problem can be circumvented by assuming a penalty which depends on k . A light penalty function can be introduced in (14) by assuming ϕ_k does not follow the relation in (4), in which case, $\boldsymbol{\psi} = [\omega_d, \omega_o, d, \rho, \theta, \sigma^2, \phi_1, \phi_2, \dots, \phi_k]^T$ and the penalty function is given by $l(k) = k + 6$. This penalty function physically pertains to a scenario, wherein the blades are not placed equidistant to one another. If this function is still not sufficient to resolve the ambiguities associated with blade number estimation, a stronger penalty can be used which assumes that all the parameters are different for each blade except the noise variance, σ^2 . This assumption then implies that $l(k) = 6k + 1$. Using the above two penalty functions in (14), one can overcome the ambiguous blade number estimation.

5. Cramér-Rao Bounds

The CRBs are necessary to analyze the performance of the proposed ML estimation algorithm. Note that the model selection is intertwined with estimation accuracy, since the negative LL costs at the ML estimates along with the penalty decide on the model selection criteria. In other words, estimation accuracy interplays with correct blade number selection, albeit in a highly nonlinear and unknown fashion. In this section, we denote the true number of blades as K . The CRB analysis in this section can be used either for the tail rotor or the main rotor blades. The combined CRBs are similar and can be derived in a straightforward manner from the results presented here. The Fisher information matrix (FIM) is defined as

F. The complete parameter vector is denoted as $\boldsymbol{\eta} = [\boldsymbol{\psi}^T, \sigma^2]^T$, where the MD parameter vector is defined as $\boldsymbol{\psi} = [\omega_d, \omega_o, d, \phi_o, \rho, \theta]^T$. The FIM elements can be derived in a compact manner for the complex Gaussian PDF due to the Slepian-Bangs formula, which is given by [18],

$$F_{\eta_r \eta_s} = \text{Tr} \left\{ \mathbf{C}^{-1} \frac{\partial \mathbf{C}}{\partial \eta_r} \mathbf{C}^{-1} \frac{\partial \mathbf{C}}{\partial \eta_s} \right\} + 2 \text{Re} \left\{ \frac{\partial \mathbf{s}}{\partial \eta_r}^H \mathbf{C}^{-1} \frac{\partial \mathbf{s}}{\partial \eta_s} \right\}, (r, s) \in (1, 2, \dots, 6) \quad (17)$$

where \mathbf{s} and \mathbf{C} denote the mean and the covariance matrix of the PDF, respectively. For our case,

$$\mathbf{s} = [s(0), s(1), \dots, s(N-1)]^T, \mathbf{C} = \sigma^2 \mathbf{I}$$

For the problem at hand, and using (17), it can be readily shown that

$$\begin{aligned} F_{\eta_r \eta_s} &= 2 \text{Re} \left\{ \mathbf{1}^T \mathbf{E}_{\psi_r}^H \mathbf{C}^{-1} \mathbf{E}_{\psi_s} \mathbf{1} \right\}, (r, s) = (1, 2, \dots, 6) \\ \mathbf{E}_{\psi_r} &\in \mathfrak{S}^{N \times K} = [\mathbf{e}_1^{\psi_r}, \mathbf{e}_2^{\psi_r}, \dots, \mathbf{e}_K^{\psi_r}] \\ \mathbf{e}_k^{\psi_r} &:= \frac{\partial}{\partial \psi_r} \boldsymbol{\beta}_k(\boldsymbol{\psi}) = \frac{\partial}{\partial \psi_r} \left(\rho e^{j\theta} \times \mathbf{h}_k(\boldsymbol{\psi}) \odot \mathbf{g}_k(\boldsymbol{\psi}) \odot \mathbf{g}_k^1(\omega_d) \right) \\ \mathbf{h}_k(\boldsymbol{\psi}) &= [h_k(0), h_k(1), \dots, h_k(N-1)]^T \\ \mathbf{g}_k(\boldsymbol{\psi}) &= [e^{j4\pi f d \cos(\phi_k)/c}, e^{j4\pi f d \cos(\omega_o(1-\phi_k)/c)}, e^{j4\pi f d \cos(\omega_o(N-1)-\phi_k)/c}]^T \\ \mathbf{g}_k^1(\omega_d) &= [1, e^{j\omega_d}, \dots, e^{j\omega_d(N-1)}]^T \\ \phi_k &= \phi_o + k2\pi / K, k = 0, 1, \dots, K-1 \end{aligned} \quad (18)$$

In (18), the vector $\mathbf{1}$ is a column vector of dimension N comprised of all ones. From hereon, we ignore the dependence of $\mathbf{h}_k(\boldsymbol{\psi})$ and $\mathbf{g}_k(\boldsymbol{\psi})$ on $\boldsymbol{\psi}$, and write them as \mathbf{h}_k and \mathbf{g}_k , respectively. The vector $\mathbf{g}_k^1(\omega_d)$ is a function of the Doppler, and hence denoted as is. The partial derivatives of $\boldsymbol{\beta}_k$ with respect to $\psi_r, r = 1, 2, \dots, 6$ are given by,

$$\frac{\partial}{\partial \theta} \boldsymbol{\beta}_k = j \boldsymbol{\beta}_k, \frac{\partial}{\partial \rho} \boldsymbol{\beta}_k = \rho^{-1} \boldsymbol{\beta}_k, \frac{\partial}{\partial \omega_d} \boldsymbol{\beta}_k = j \mathbf{n} \odot \boldsymbol{\beta}_k, \mathbf{n} := [0, 1, 2, \dots, N-1]^T \quad (19)$$

$$\begin{aligned}
\frac{\partial}{\partial \omega_o} \mathbf{p}_k &= \rho e^{j\theta} \left(\frac{\partial \mathbf{h}_k}{\partial \omega_o} \odot \mathbf{g}_k \odot \mathbf{g}_k^1 + \mathbf{h}_k \odot \mathbf{g}_k \odot \mathbf{n} \odot \text{Im}\{\xi_k\} \odot \mathbf{g}_k^1 \times \frac{-j4\pi fd}{c} \right) \\
\xi_k &:= [1, e^{j\omega_o}, e^{2j\omega_o}, \dots, e^{j(N-1)\omega_o}]^T \times e^{-j\phi_k} \\
\frac{\partial \mathbf{h}_k}{\partial \omega_o} &:= \begin{pmatrix} \text{Re}\{\mathbf{g}_k\} \odot \frac{-4\pi fd}{c} \mathbf{n} \odot \text{Im}\{\xi_k\} \odot \frac{4\pi fd}{c} \text{Re}\{\xi_k\} \\ -\text{Im}\{\mathbf{g}_k\} \odot \frac{-4\pi fd}{c} \mathbf{n} \odot \text{Im}\{\xi_k\} \end{pmatrix} \odot (\mathbf{v}^{\odot -2}) \\
\mathbf{v} &:= \frac{4\pi fd}{c} \text{Re}\{\xi_k\}
\end{aligned} \tag{20}$$

where $(\cdot)^{\odot -k}$ is defined as the elementwise division of a vector or a matrix raised to k -th power, i.e., if $\mathbf{x} = [x_1, x_2, \dots, x_N]^T$, then $\mathbf{x}^{\odot -k} = [1/x_1^k, 1/x_2^k, \dots, 1/x_N^k]^T$. Using the same notation, the other derivatives which are required for evaluating the FIM are provided below.

$$\begin{aligned}
\frac{\partial}{\partial d} \mathbf{p}_k &= \rho e^{j\theta} \left(\frac{\partial \mathbf{h}_k}{\partial d} \odot \mathbf{g}_k \odot \mathbf{g}_k^1 + \mathbf{h}_k \odot \mathbf{g}_k \odot \text{Re}\{\xi_k\} \odot \mathbf{g}_k^1 \times \frac{j4\pi f}{c} \right) \\
\frac{\partial \mathbf{h}_k}{\partial d} &:= \begin{pmatrix} \text{Re}\{\mathbf{g}_k\} \odot \frac{4\pi f}{c} \text{Re}\{\xi_k\} \odot \frac{4\pi fd}{c} \text{Re}\{\xi_k\} \\ -\text{Im}\{\mathbf{g}_k(\Psi)\} \odot \frac{4\pi f}{c} \text{Re}\{\xi_k\} \end{pmatrix} \odot (\mathbf{v}^{\odot -2})
\end{aligned} \tag{21}$$

$$\begin{aligned}
\frac{\partial}{\partial \phi_o} \mathbf{p}_k &= \rho e^{j\theta} \left(\frac{\partial \mathbf{h}_k}{\partial \phi_o} \odot \mathbf{g}_k \odot \mathbf{g}_k^1 + \mathbf{h}_k \odot \mathbf{g}_k \odot \text{Im}\{\xi_k\} \odot \mathbf{g}_k^1 \times \frac{j4\pi fd}{c} \right) \\
\frac{\partial \mathbf{h}_k}{\partial \phi_o} &:= \begin{pmatrix} \text{Re}\{\mathbf{g}_k\} \odot \frac{4\pi fd}{c} \text{Im}\{\xi_k\} \odot \frac{4\pi fd}{c} \text{Re}\{\xi_k\} \\ -\text{Im}\{\mathbf{g}_k\} \odot \frac{4\pi fd}{c} \text{Im}\{\xi_k\} \end{pmatrix} \odot (\mathbf{v}^{\odot -2})
\end{aligned} \tag{22}$$

Since the covariance matrix is not a function of Ψ , the cross FIM elements with respect to σ_i^2 and all the parameters in Ψ are zero, i.e.,

$$F_{\sigma_i^2 \Psi_r} = 0, \quad r = (1, \dots, 6) \tag{23}$$

Therefore, the CRBs depend only on the inverted FIM of the MD parameters. The CRBs are evaluated numerically in the simulation section.

6. Simulation and Experimental Results

6.1. Simulation

In this section, we present parameter and blade number estimation results for a variety of operating conditions. The number of Montecarlo trials is set to 200, unless otherwise stated, and the carrier frequency is set at 900MHz. We evaluate pseudo ML for each consecutive integer blade number up to a maximum of 8, regardless of whether the target has even or odd number of blades. This procedure is adopted for ease of exposition. In practice, however, the TF signature of the returns can guide the decision of the blade number being even or odd, and then the ML needs to be evaluated only for even or odd blade counts. The SNR is defined as $\|\mathbf{s}\|^2 / N\sigma^2$, unless mentioned otherwise. The AIC corresponding to the penalty functions $l(k)=7$, $l(k)=k+6$, and $l(k)=6k+1$, are denoted as AIC1, AIC2, and AIC3, respectively. Likewise, for the MDL.

6.1.1. All parameters assumed known and no clutter

The ML algorithm is initialized with the true parameters, and the empirical probabilities for the ITCs are shown in the Fig. 9. The results pertinent to AIC and MDL are depicted in the left and the right columns, respectively. The x-axis in the sub-plots represents the blade number, and the y-axis is the SNR from -5dB to 25dB in 5dB increments. The true number of main rotor blades is 3. We observe that both AIC1/AIC2 pick 6 blades with an overwhelming majority. On the other hand, AIC3, which has the strongest penalty associated with it, picks the correct number of blades with an overwhelming majority. Furthermore, while MDL1 provides performance similar to AIC1, MDL2 performs much better than AIC2, and is second only to MDL3, which yields perfect blade number estimates. Noting that the simulation is the ideal case corresponding to initialization of the ML with the true parameters, two inferences can be made. Firstly, the blade number selection is indeed ambiguous, and secondly, the designed penalty functions perform satisfactorily. For the simulation, the sampling frequency is 2 kHz, ω_d is $72.6 \times 2\pi$ Hz, the rotation rate is 100Hz, with parameters $d=3\text{m}$, and $\phi_o = \pi/8$. The data length

used corresponds to 1024 samples. Higher Doppler frequencies were not considered in order to reduce the computational complexity of the procedure. To validate the CRB derivations, the mean square error (MSE) of the estimates is shown in the Fig. 10. We observe that in all cases, the MSE is close to the CRB, which serves as corresponding lower bound.

6.1.2. Unknown parameters with clutter filter

The signal parameters and the range of SNRs are the same as in section 6.1.1. The number of main rotor blades, however, is chosen to be 4. The normalized bandwidth of the clutter filter is assumed to be $\pm 0.05 \times 2\pi$. The performance of the various ITCs is shown in Fig 11. From the figure, it is clear that MDL3 gives the best performance. It is noted that the performance of AIC1/AIC2 and MDL1/MDL2 is better in this case than their corresponding performances in Fig 9. This is because, for Fig. 9, the ML was initialized with the same parameters for every hypothesized blade. In Fig. 11, however, the initialization parameters for the PML are different for different hypothesized blade numbers; hence the difference in performance. The MSE of the parameters corresponding to the true blade number along with the MSE of the suboptimal estimates are shown in Fig. 12. Unlike Fig. 10, the estimates for the correct blade number are above the CRBs. We further note that the MSE of the suboptimal estimates for ω_d and d are very close to the MSE of the corresponding PML estimates (See Fig. 12(a, c)). In fact, for some low SNR values, the PML MSE for both ω_d and d are slightly higher than the corresponding suboptimal MSE. This can be attributed to the presence of the clutter filter. The MSE for an incorrect blade number selection of 8 is also provided in Fig. 12 for comparison. As expected, the MSE of the estimates for 8 blades are much higher than the MSE of the true parameters, except the Doppler frequency. The suboptimal Doppler estimate does not depend on the hypothesized blade count, and hence the Doppler MSE for both the correct and incorrect blade numbers are similar.

Fig. 13 shows the empirical probabilities of correct blade number selections when the SNR is fixed at 10dB, and the clutter filter bandwidth is varied. Only the positive clutter bandwidths are shown along the y-axis as the clutter filter has a symmetric frequency response, and the x-axis denotes the hypothesized

blade count. As expected, the probability of correct blade number selection decreases with increasing clutter filter bandwidth. MDL3 outperforms the other ITCs, although like the rest its performance deteriorates when the bandwidth increases.

6.2. Experimental results

The data used in this section is identical to the helicopter data used in [3]. The data comprises of pulse Doppler radar returns of a helicopter with a 5-blade main rotor and a 6-blade tail rotor. It is known that the helicopter was hovering at a range of 2500m, and at a height of 60m above the ground [3]. Due to the sensitive nature of the data, the experimental details such as carrier frequency, the type of the helicopter, its shape and blade structure, the shape of the pulses used, and the pulse repetition rate, was not disclosed to us. It is only known that the radar operates in the X-band. The data consists of the complex samples after matched filtering at range gates at which the helicopter was present. For our analysis, it is immaterial to know the precise carrier frequency, as it is simply a multiplicative factor in the phase. Hence, we pick 10 GHz from the X-band as the carrier frequency and use it for analysis. The knowledge of other parameters is not required. The return from the helicopter main body is removed by a clutter filter whose normalized bandwidth is $(\pm) 0.01 \times 2\pi$. In Fig. 14(a), the spectrogram of the data after clutter filtering is shown and in Fig. 14(b-c), the spectrograms of the data after excising the main and tail rotor components using the proposed FrFT procedure are shown. Furthermore, it is seen from Fig. 14(b) that the main rotor signal is aliased as evidenced from the signal folding across the negative and positive frequencies in the spectrogram. The aliasing is not evident in Fig. 14(a) as the main rotor signal was masked by the strength of the tail rotor signals. From the spectrograms, we can verify that the tail rotor has an even number of blades, and the main rotor has an odd number of blades.

One can also see from Fig. 14(b) and Fig. 14(c) that the main rotor has a lower strength than the tail rotor. This phenomenon is due to a variety of reasons. First, the assumptions that the main rotor blades are rigid homogenous rods are a simplification for modeling rotor blades [9-11]. In reality, the main rotor consists of blades which have both camber and twist. The tail rotor, on the other hand, in most cases

follows the modeling assumptions. Second, at certain aspect angles, due to the camber and twist of the main rotor blades, most of the transmitted signal energy is spread out in directions away from the radar. On the other hand, for the same aspect angles, since the tail rotor plane of rotation is perpendicular to the plane of rotation of the main rotor, it is more or less seen perpetually by the radar. Hence, the tail rotor returns appears stronger than the main rotor, even though physically the tail blade has a smaller cross section than the main rotor blade. This is explained in more detail in [15]. Another plausible explanation is that the radar used a highly directive antenna which focused energy on the tail rotor only, and the returns from the main rotor were welcomed in the antenna sidelobes causing it to have a lower RCS.

The results of the PML applied to the experimental data are consistent with the ground truth for the tail rotor. However, the number of blades in the main rotor was estimated to be 3 instead of 5. This inconsistency can be attributed to the low RCS of the main blades. Also, the aliasing effect of the main rotor blades could possibly confuse the PML in picking incorrect estimates. More advanced simulations are required to verify this conjecture, which is beyond the scope of the paper. Fig. 15 shows the spectrograms (with normalized amplitudes) of the hypothesized signals for the tail rotor corresponding to 6 and 8 blades along with the measured tail rotor signal's spectrogram. The hypothesized spectrograms for 2 and 4 blades were observed to be drastically different from the measured 6-blade spectrogram, and are not shown due to lack of space. We observe that, although both the hypothesized spectrograms are similar to that in Fig. 15(a), the spread in the frequency of the flashes in Fig. 15(c) is larger than the true spread in Fig. 15(a). The ITCs judiciously select 6 blades as the blade number estimate. Fig. 16 shows the spectrograms (with normalized amplitudes) of the hypothesized main rotor blades corresponding to 3, 5 and 7 blades along with the measured main rotor signal's spectrogram. The hypothesized spectrograms for 3 and 5 blades are similar to the measured spectrograms, while the spectrogram in Fig. 16(d) is different from that in Fig. 16(a). More specifically, consider the blade flash closest to the 1500th sample in Fig. 16(a). This blade flash is misaligned temporally in Fig. 16, whereas it is perfectly aligned for the 3 and 5 blade spectrograms. Hence one can reject the 7 blade conjecture. We further observe from Fig. 16(b-c) that for the 3 blade spectrogram, the aliasing is captured by the hypothesized signal and is more or less identical to the aliasing

as seen in Fig. 16(a). However, in the 5 blade spectrogram, the signal aliasing as captured by the PML is severe and much more than the true aliasing present in Fig. 16(a). This extra degree of aliasing may have caused the log likelihood cost to degrade, and the ITCs penalize the 5 blade spectrogram more severely than what was desired, resulting in a blade number estimate of 3.

7. Conclusions

In this paper, we analyzed the radar returns for a helicopter for parameter estimation and blade number selection. A Doppler radar with unmodulated carrier is considered. The ML estimation algorithm was derived and its performance, compared to CRB, was examined through computer simulations and real data measurements. Several information theoretic criteria were considered for blade number selections. It is shown that these ITCs yield in most cases incorrect blade numbers. The ambiguity of such estimates can be alleviated by using specialized ITC penalties. For the problem at hand, we showed the significance of using FrFT, in terms of reduced complexity signal separation and Doppler estimation. Experimental data from a pulse Doppler radar was used to validate the proposed parameter estimation approach for helicopter blade numbered rotational characteristics.

ACKNOWLEDGMENT

We are thankful to Dr. Thayaparan Thayanathan from DRDC, Ottawa, Canada, for providing the experimental pulse-Doppler data.

REFERENCES

- [1] V. C. Chen, F. Li, S. -S. Ho, and H. Wechsler, "Analysis of micro-Doppler signatures," *IEEE Radar Sonar, and Navig.*, vol. 150, no. 4, pp. 271-276, Aug. 2003.
- [2] V. C. Chen, F. Li, S.-S. Ho, H. Wechsler, "Micro-Doppler effect in radar: Phenomenon, model, and simulation study," *IEEE Trans. Aerospace and Electron. Sys.*, vol. 42, no. 1, pp. 2-21, Jan. 2006.

- [3] T. Thayaparan, S. Abrol, E. Riseborough, L.J. Stankovic, D. Lamothe, and G. Duff, "Analysis of radar micro-Doppler signatures from experimental helicopter and human data," *IET Radar Sonar and Navig.*, vol. 1, no.4, pp. 289-299, Aug. 2007.
- [4] G. Greneker, J. Geisheimer, and D. Asbell, "Extraction of micro-Doppler from vehicle target at X-band frequency," *Proc. SPIE Radar Sensor Tech. VI*, vol. 4374, pp. 1-9, Orlando, FL, 19-23 Apr. 2001.
- [5] M. R. Bell, and R. A. Grubbs, "JEM modeling and measurement for radar target identification," *IEEE Trans. Aerospace and Electron. Sys.*, vol. 29, no. 1, pp. 73-87, Jan. 1993.
- [6] P. Tait, *Introduction to Radar Target Recognition*, Institution of Engineering and Technology, London, UK, 2006.
- [7] R. J. Wellman, and J. L. Silvius, "Doppler signature measurements of an Mi-24 Hind-D helicopter at 92 GHz", Army Research Laboratory Report, ARL-TR-1637, Adelphi, MD, 1998.
- [8] B. D. Bullard, and P. C. Dowdy, "Pulse Doppler signature of a rotary-wing aircraft," *IEEE Aerospace and Electron. Sys. Magazine*, vol. no. pp. 28-30, May 1991.
- [9] V. C. Chen, and H. Ling, *Time-Frequency Transforms for Radar Imaging and Signal Analysis*, Artech House, Boston, 2002.
- [10] S. L. Marple Jr., "Large dynamic range time-frequency signal analysis with application to helicopter doppler radar data," *In Proc. Int'l Symposium of Signal Processing and its Applications*, Kuala Lumpur, Malaysia, Aug. 13-16, pp. 260-263, 2001.
- [11] J. G. Leishman, *Helicopter Dynamics*, Cambridge University Press, Cambridge UK, 2000
- [12] J. Martin and B. Mulgrew, "Analysis of the theoretical radar return signal from aircraft propeller blades," *Proc. IEEE Radar Conf.*, Arlington, VA, May 7-10, pp. 569-572, 1990.
- [13] H. Schneider, "Application of an autoregressive reflection model for the signal analysis of radar echoes from rotating objects," *Proc. Int. Conf. Acoust., Speech, Signal Process.*, New York, NY, Apr. 11-14, vol. 2, pg. 1236-1239, 1988.

- [14] J. Misiurewicz, K. Kulpa, and Z. Czekala, "Analysis of recorded helicopter echo," *In Proc. IEEE National Radar Conf.*, Edinburgh, May 13-15, pp. 449-453, 1997.
- [15] T. Johnsen, K. E. Olsen, and R. Gundersen, "Hovering helicopter measured by bi-/multistatic CW radar," *Proc. IEEE Radar Conf.*, Huntsville, AL, May 5-8, pp. 165-170, 2003.
- [16] Y. Sang-Ho, K. Byungwook, and K. Young-Soo, "Helicopter classification using time-frequency analysis," *Electronics Letters*, vol. 36, no. 22, pp. 1871-1872, Oct. 2000.
- [17] A. Cilliers, and W. Nel, "Helicopter paramter extraction using joint time-frequency and tomographic techniques," *Proc. IEEE Radar Conf.*, Rome, Italy, May 26-30, pp. 598-603, 2008.
- [18] S. M. Kay, *Fundamentals of Statistical Signal Processing, Volume: II, Estimation Theory*, Prentice Hall, Englewood Cliffs, NJ, 1993.
- [19] C. Gourieroux, A. Monfort, and A. Trognon, "Pseudo maximum likelihood methods:Theory," *Econometrica*, vol. 52, no. 3, pp. 681-700, May 1984.
- [20] F. Gini, and G. B. Giannakis, "Hybrid FM-polynomial phase signal modeling: parameter estimation and Cramér-Rao bounds," *IEEE Trans. Signal Process.*, vol. 47, no. 2, pp. 363-377, 1999.
- [21] M. G. Christensen, A. Jakobsson and S. H. Jensen, "Joint high-resolution fundamental frequency and order estimation," *IEEE Trans. on Audio, Speech and Language Processing*, vol. 15, no. 5, pp. 1635-1644, Jul. 2007.
- [22] L. B. Almeida, "The Fractional Fourier transform and time frequency representations," *IEEE Trans. Sig. Proc.*, vol. 42, no. 11, pp. 3084-3091, Nov. 1994.
- [23] G. F. Boudreaux-Bartels, and T. W. Parks, "Time-varying filtering and signal estimation using Wigner distribution synthesis techniques," *IEEE Trans. Acoust. Spech and Sig. Proc.*, vol. ASSP-34, no. 3, pp. 442-451, Jun. 1986.
- [24] F. Hlawatsch, and W. Krattenthaler, "Bilinear signal synthesis," *IEEE Trans. Sig. Proc.*, vol. 40, no. 2, pp. 352-363, Feb. 1992.

- [25] H. M. Ozaktas, O. Arikan, M. A. Kutay, and G. Bozdađı, “Digital computation of the fractional Fourier transform,” *IEEE Trans. Sig. Proc.*, vol. 44, no. 9, pp. 2141-2150, Sep. 1996.
- [26] A. M. Zoubir, and D. R. Iskander, *Bootstrap Techniques for Signal Processing*, Cambridge Univ. Press, Cambridge, UK, 2004.
- [27] H. Akaike, “A new look at the statistical model identification,” *IEEE Trans. Automatic Control*, vol. 19, no. 6, pp. 716-723, 1974.
- [28] G. E. Schwarz, “Estimating the dimension of a model,” *Annals of Statistics*, vol. 6, no. 2, pp. 461-464, 1978.
- [29] J. Rissanen, “Modeling by shortest data description,” *Automatica*, vol. 14, pp. 465-471, 1978.
- [30] M. Wax, and T. Kailath, “Detection of signals by information theoretic criteria,” *IEEE Trans. Acoustics, Speech, and Signal Process.*, vol. ASSP-33, no. 2, pp. 387-392, Apr. 1985.
- [31] A. D. Lanterman, “Schwarz, Wallace, and Rissanen: Intertwining themes in theories of model selection,” *International Statistical Review*, vol. 69, no. 2, pp. 185-212, Aug. 2001.

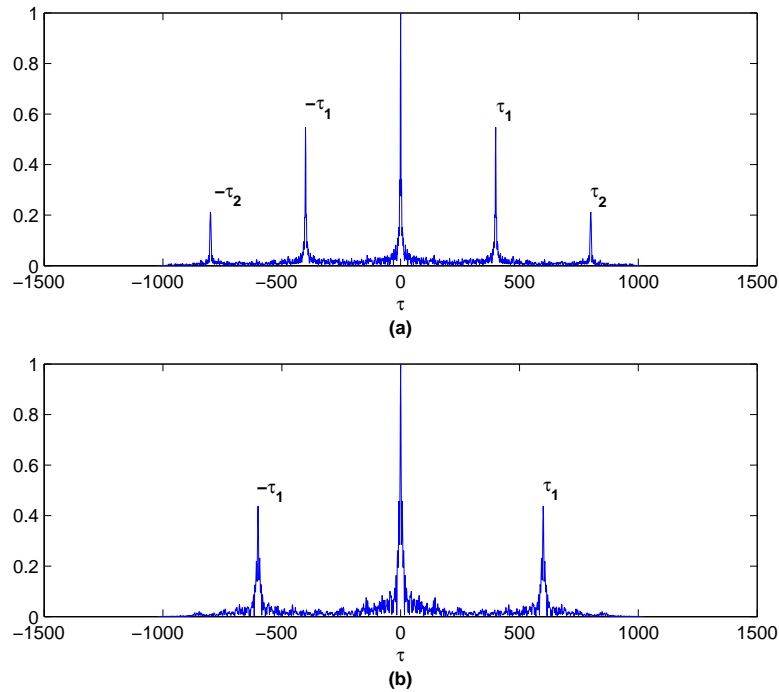


Fig. 1 Correlation sequence showing the peaks, (a) 3 blade helicopter, (b) 4 blade helicopter. Figures were generated after clutter filtering with SNR at 10dB. X-axis represents the discrete lags, and the y-axis denotes the magnitude of the normalized correlation.

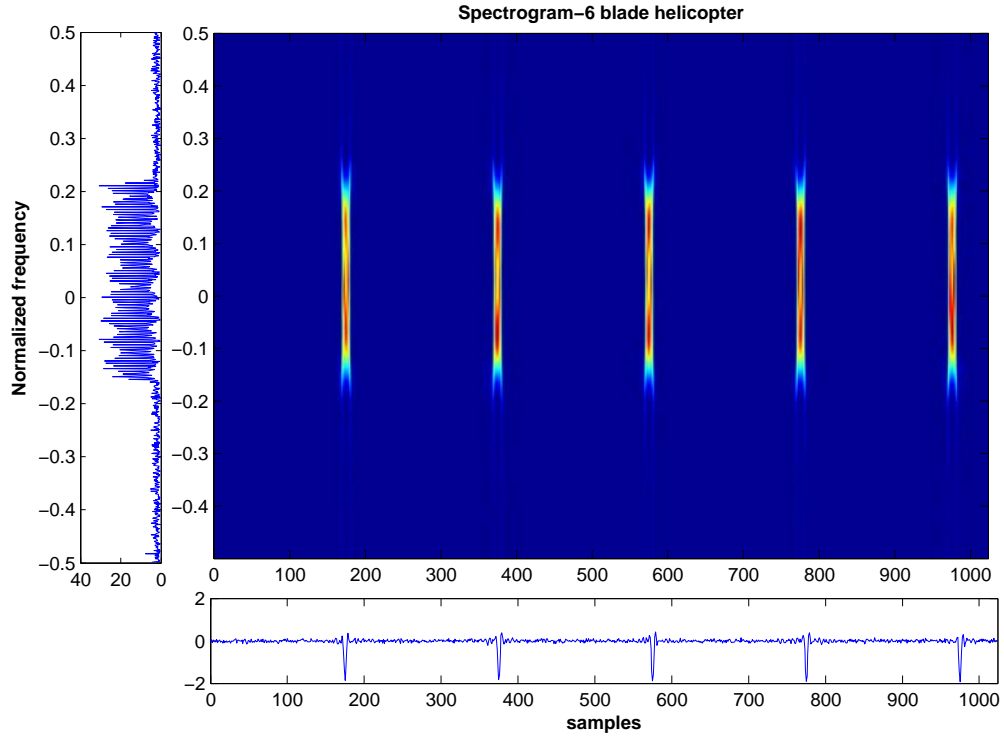


Fig. 2 (a) Six blade helicopter in 10dB noise, spectrogram is shown. Notice that the noise outside the signals frequency support is hardly seen in the TF plane. No clutter is assumed.

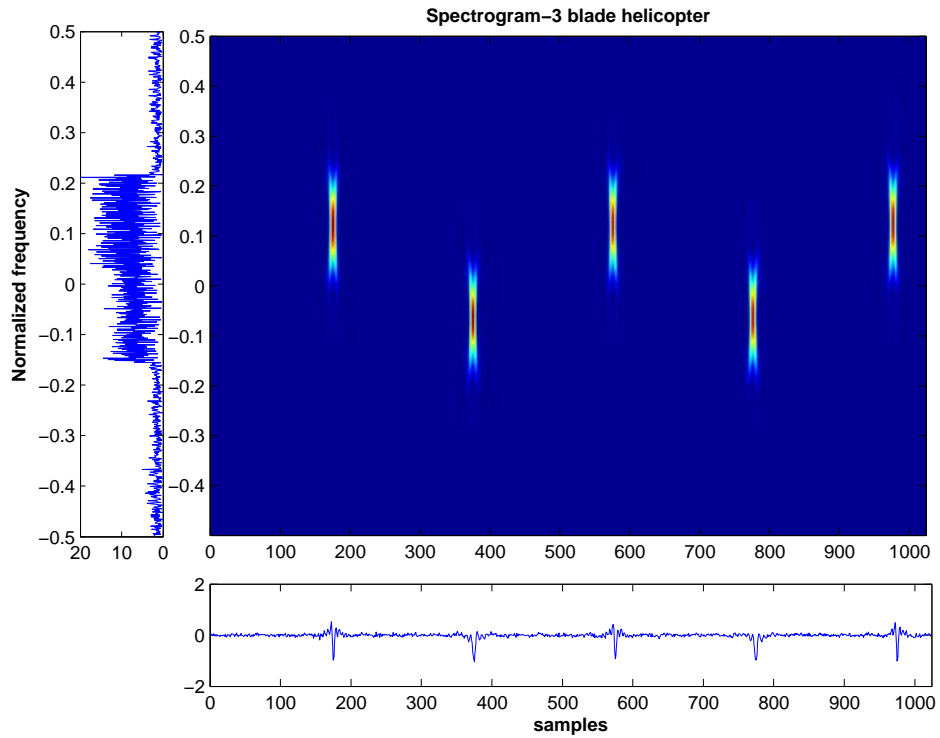


Fig. 2 (b) Three blade helicopter in 10dB noise, spectrogram is shown. Notice that the noise outside the signals frequency support is hardly seen in the TF plane. No clutter is assumed.

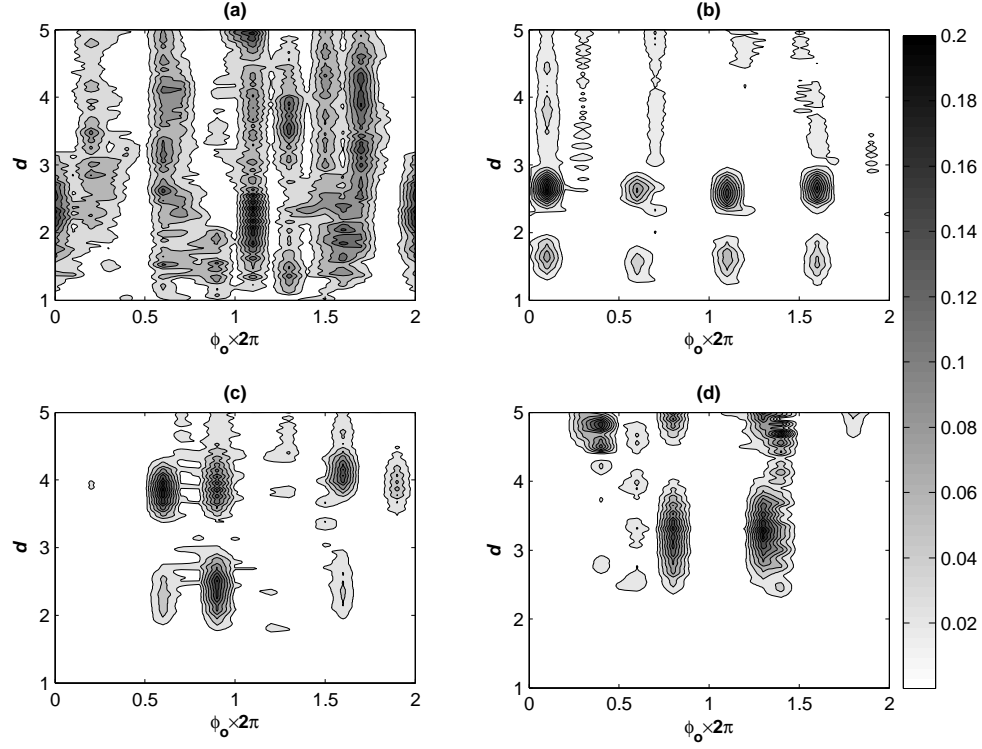


Fig. 3 Four blade helicopter in 5dB noise and the clutter bandwidth is (+/-)0.001 normalized frequency, the cost function in eq. (10) for (a) 2-blades, (b) 4 blades, (c) 6 blades, and (d) 8 blades.

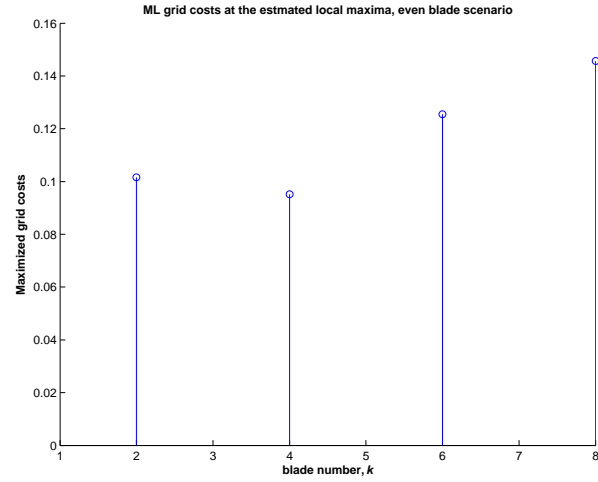


Fig. 4 Four blade helicopter in 5dB noise and the clutter bandwidth is (+/-)0.001 normalized frequency, the estimated grid costs. For this case blindly using eq. (12) results in picking 8 blades.

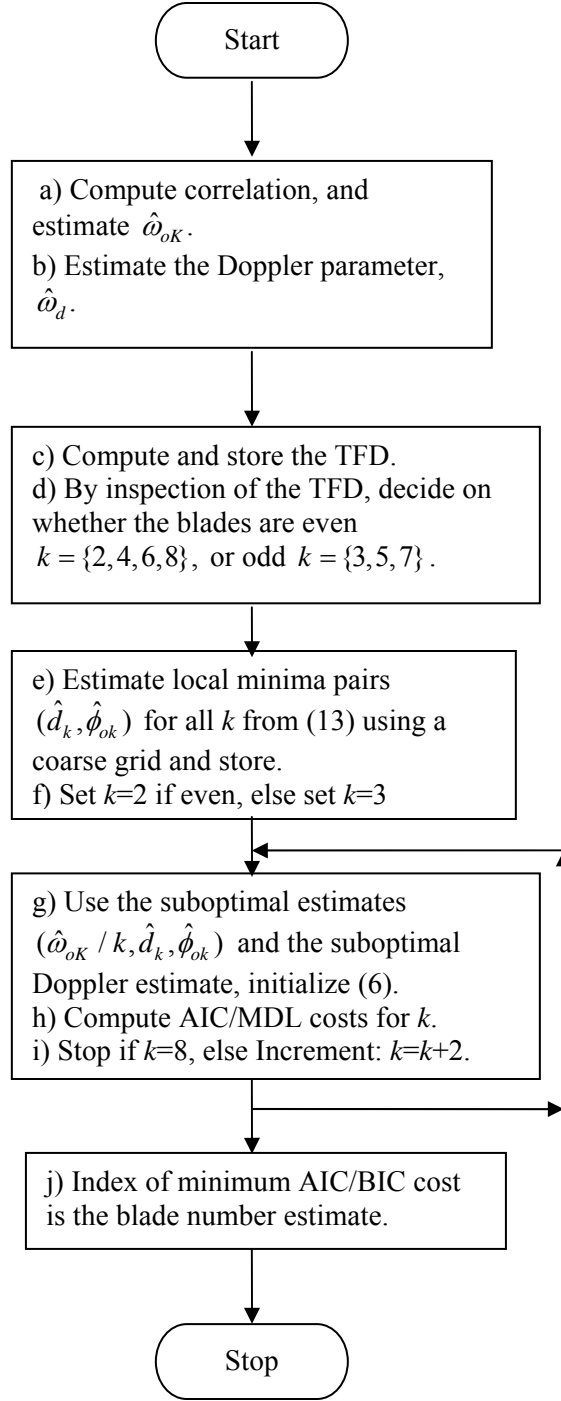


Fig. 5 Flowchart.

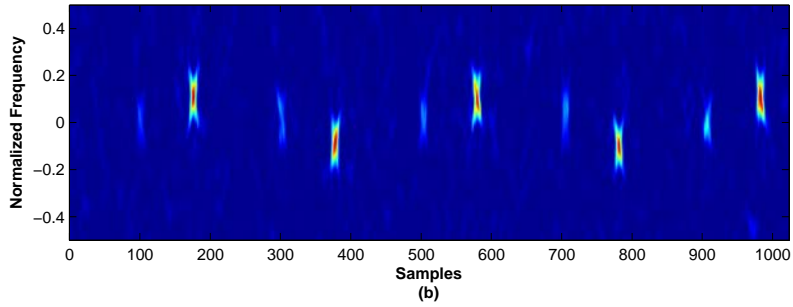
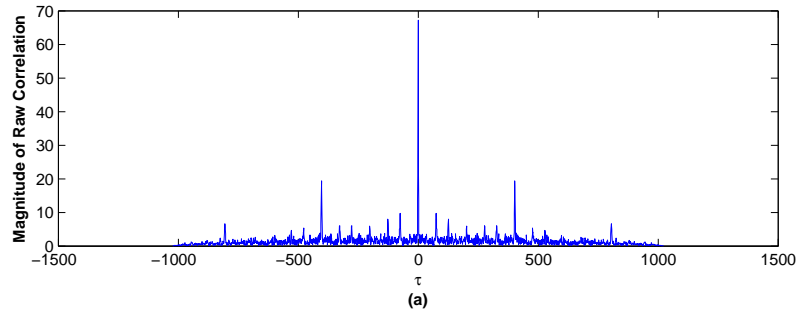


Fig. 6 (a) Correlation of signal with main and tail rotor, (b) spectrogram

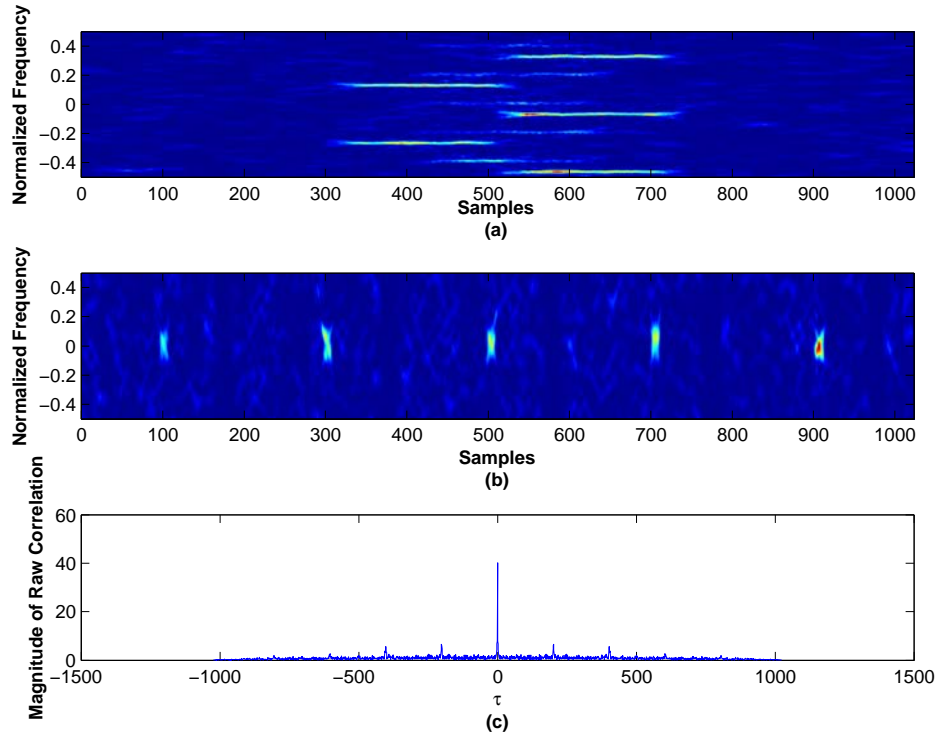


Fig. 7 (a) spectrogram of FrFTed signal in Fig. 6, (b) after excision of main rotor signal and inverse FrFT, (c) correlation of the resulting signal.

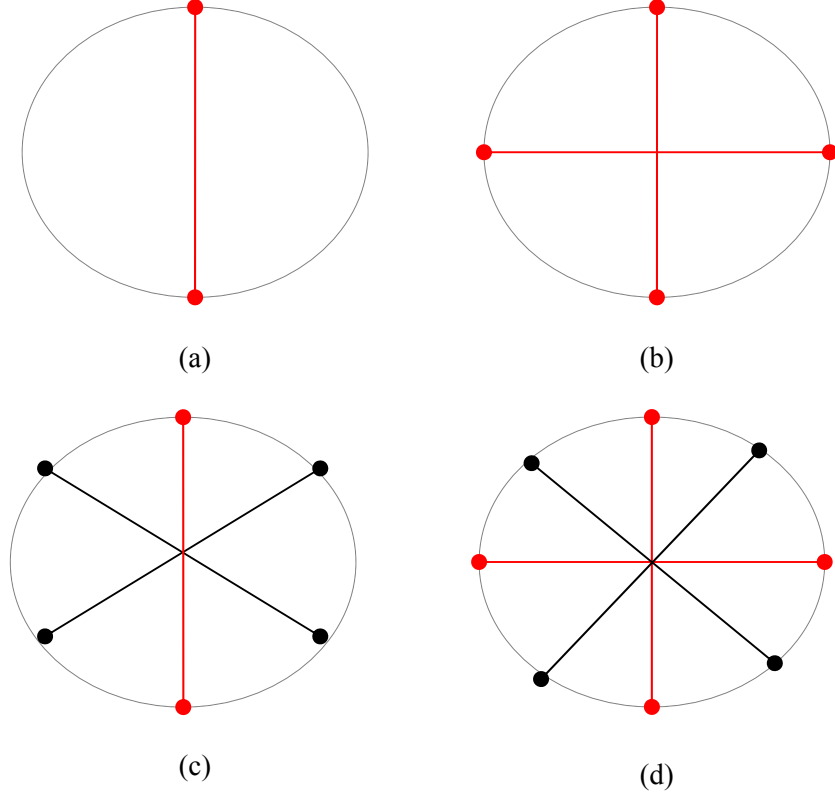


Fig. 8 Representative blade positions at rest for (a) $K = 2$, (b) $K = 4$, (c) $K = 6$, and (d) $K = 8$.

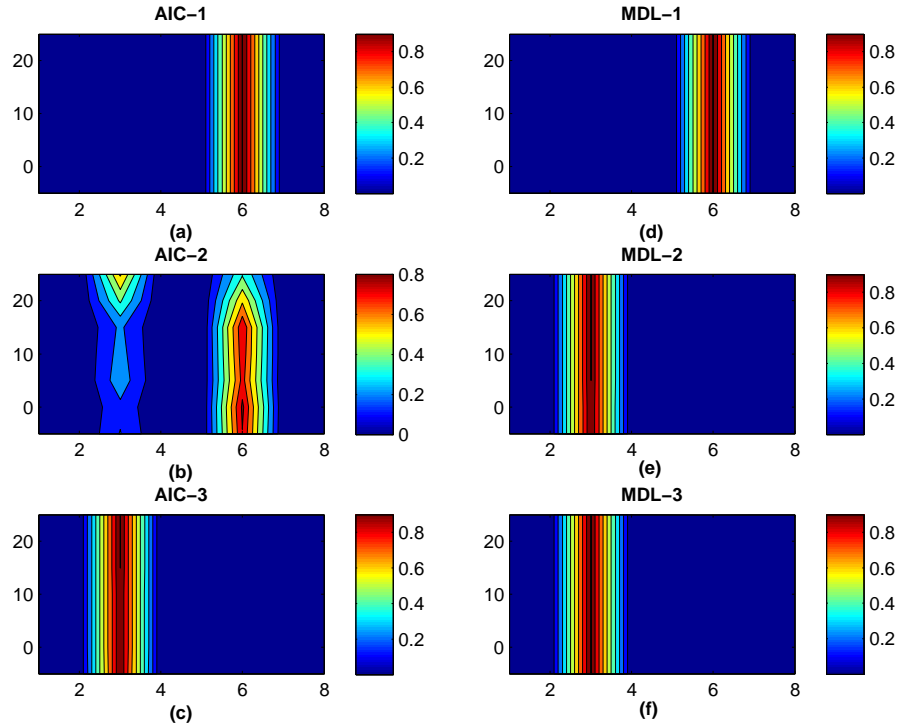


Fig. 9 Simulation with 3 main blades for illustrating the ITCs when all parameters are known. In each plot, the x-axis is the hypothesized blade number, and y-axis is the SNR in dB.

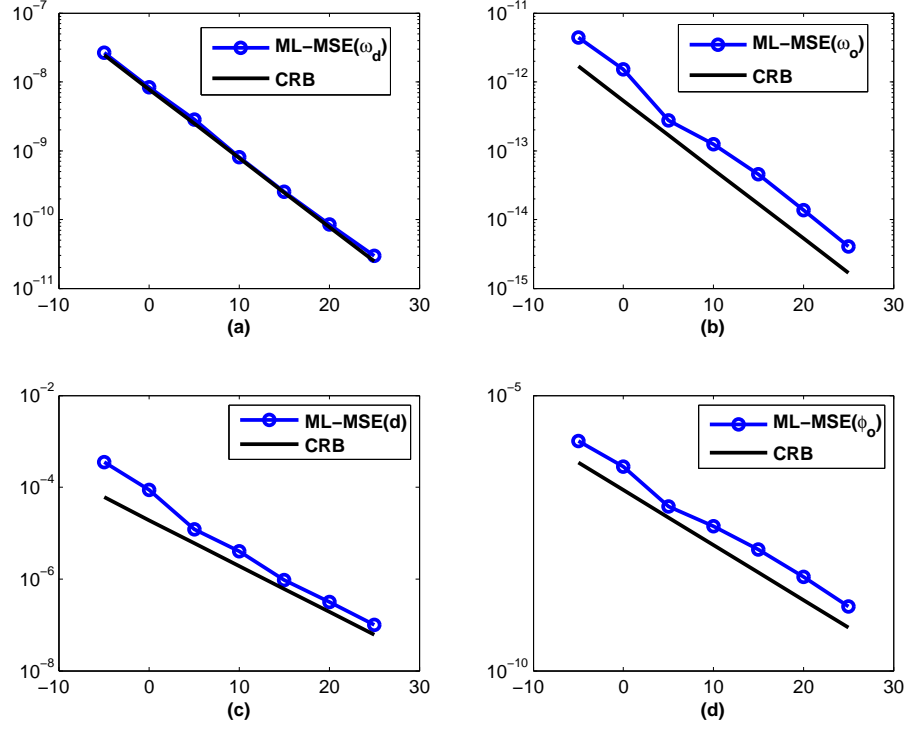


Fig. 10 MSE of the parameters at the true blade number initialized with the true parameters. (a) ω_d , (b) ω_o , (c) d , and (d) ϕ_o . In each plot, x-axis is the SNR in dB, and y-axis is the MSE.

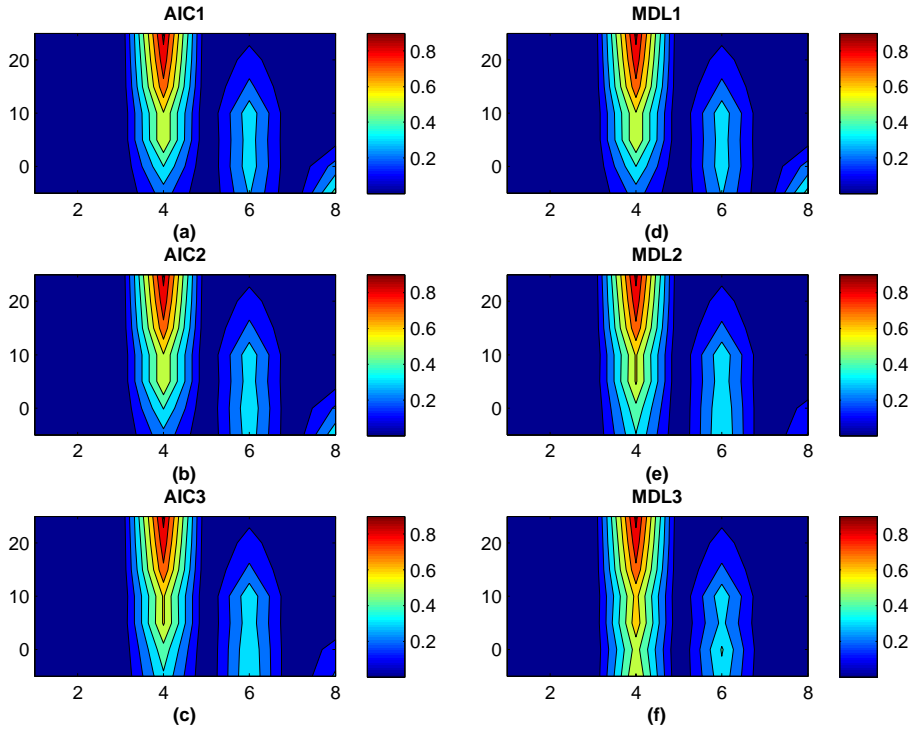


Fig. 11 Simulation with clutter filter and performance of ITCs for 4 main blades. In each plot, x-axis is the hypothesized blade number, and y-axis is the SNR in dB.

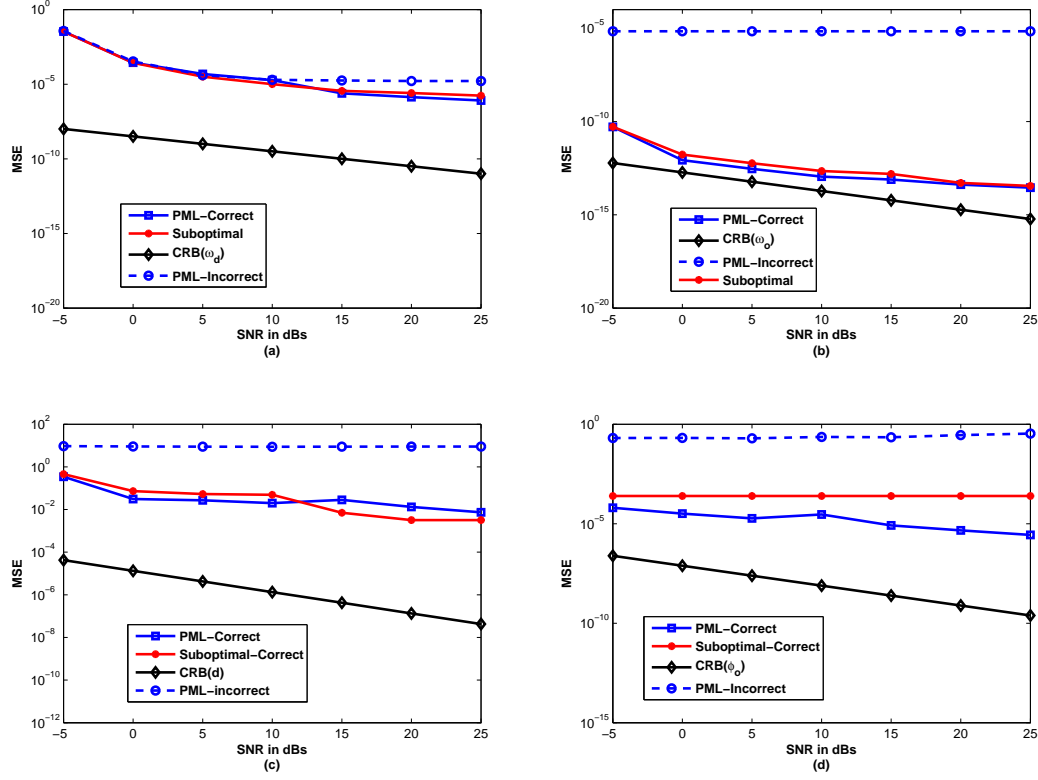


Fig. 12 MSE of the PML and CRBs vs. SNR for the true blade number and an incorrect blade number of 8, for parameters (a) ω_d , (b) ω_o , (c) d , and (d) ϕ_o .

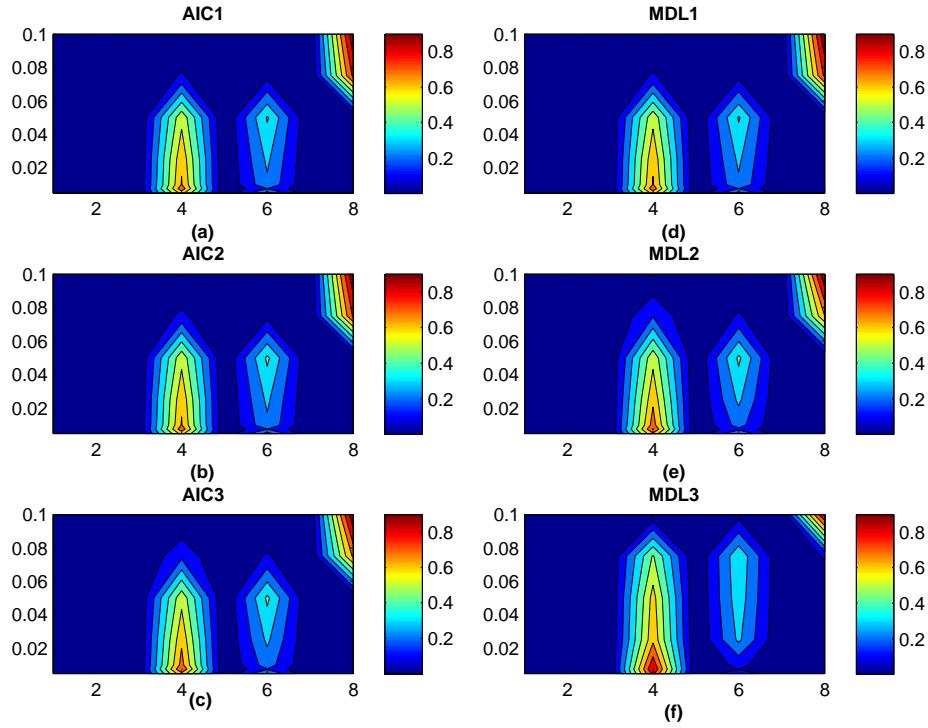


Fig. 13 Simulations to compare ITCs vs. bandwidth of the clutter filter. In each plot, x-axis is the hypothesized blade number, and y-axis is the positive bandwidth of the symmetric clutter filter.

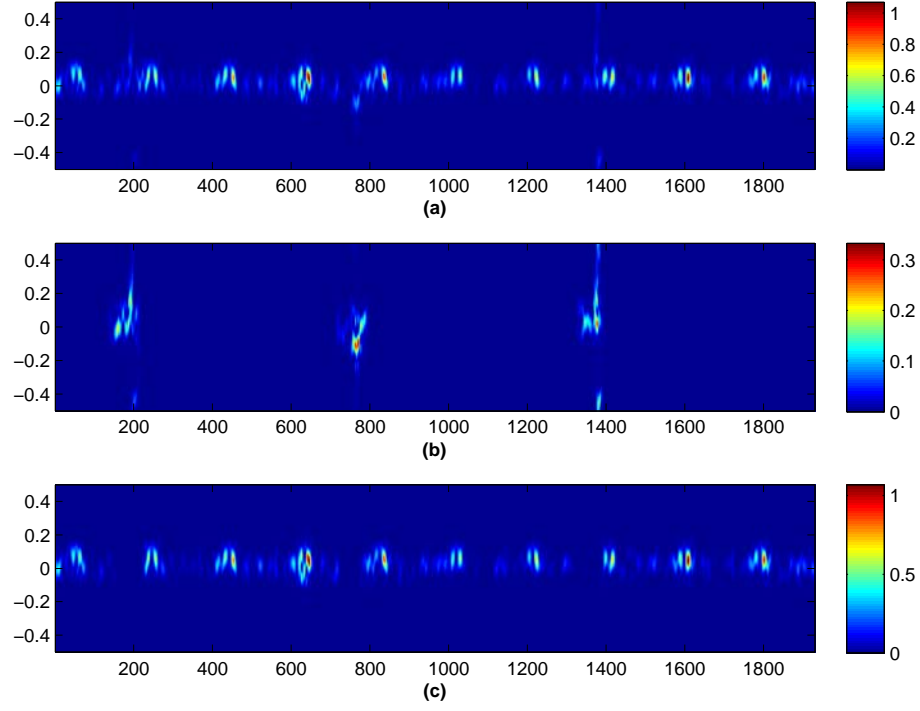


Fig. 14 Spectrograms of: (a) original experimental data, (b) main rotor excised data using FrFT, and (c) tail rotor excised data using FrFT. The x-axis is the discrete time samples, and y-axis is the normalized frequency.

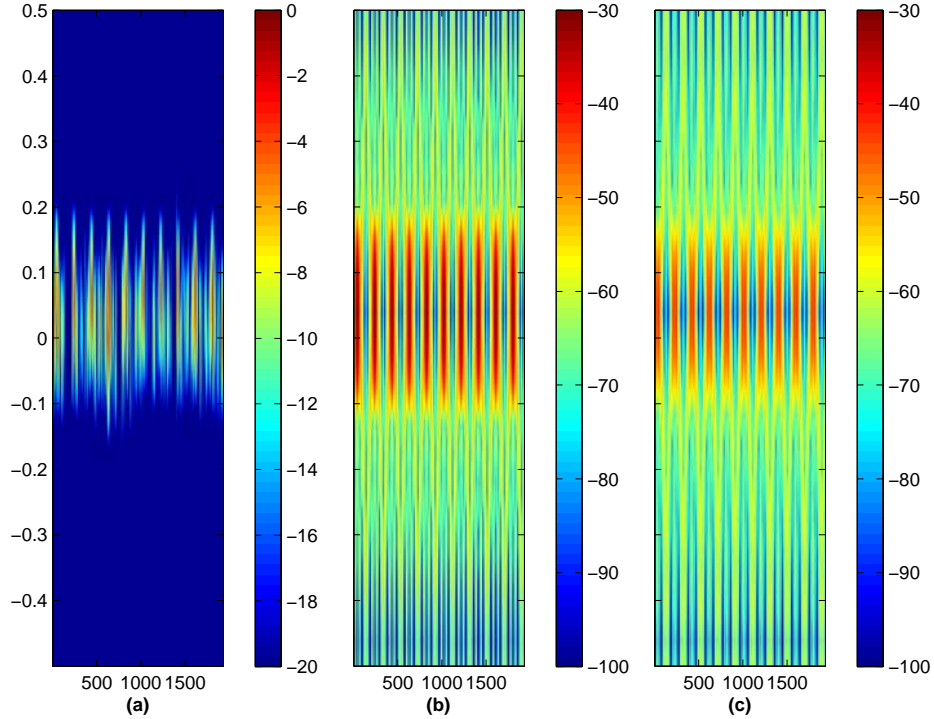


Fig. 15 Tail rotor signal spectrograms, (a) measured after FrFT, (b) 6 blade hypothesized, and (c) 8 blades. The x-axis is the discrete time in samples, and y-axis is the normalized frequency.

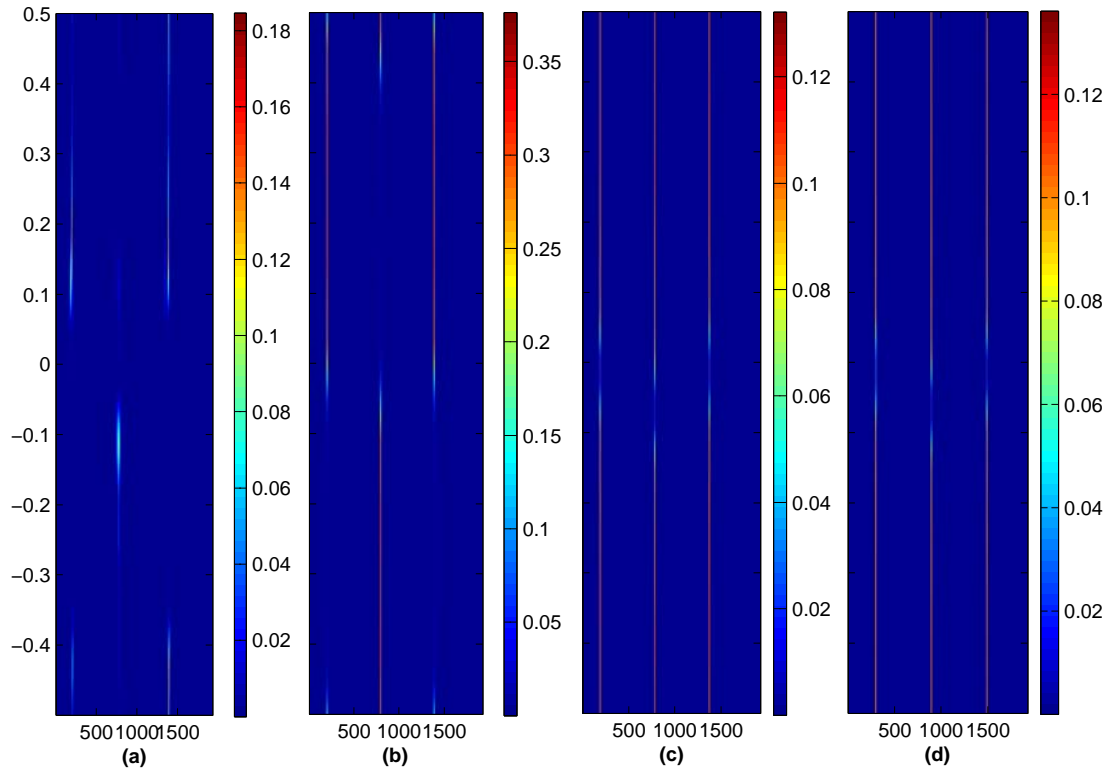


Fig. 16 Hypothesized main rotor signal spectrograms, (a) measured spectrogram after FrFT, (b) 3 blades, (c) 5 blades, and (d) 7 blades. The x-axis is the discrete time in samples, and y-axis is the normalized frequency.